Front. Earth Sci. 2014, 8(1): 18–31
DOI 10.1007/s11707-013-0400-0

RESEARCH ARTICLE

Estimating the impact of land use change on surface energy partition based on the Noah model

Shaohui CHEN (✉)[1], Hongbo SU[1], Jinyan ZHAN[2]

1 Key Laboratory of Water Cycle and Related Land Surface Processes, Institute of Geographical Sciences and Natural Resources Research, Chinese Academy of Sciences, Beijing 100101, China
2 School of Environment, Beijing Normal University, Beijing 100875, China

Abstract It is well known that land use has an important impact on surface energy partition. It is important to study the evolving trend of the partition of sensible heat flux (SHF) and latent heat flux (LHF) from the net radiance (NR) with land use change in the context of regional climate changes. In this paper, we studied the response of energy partition to land use using the Noah model. First, the Noah model simulation results of SHF and LHF between 2003 and 2005 were comprehensively validated using the observation data from the Changbai Mountain Station, the Xilinhot Station, and the Yucheng Station. The study domains represent three different types of land use change: excessive deforestation, grassland degeneration aggravation, and groundwater level decline, respectively. The study period was subsequently extended from 2015 through 2034, using four projected land use maps and forcing data from Princeton (2000–2004). The simulation results show that during the land use conversions, the annual average of LHF drops by 10.7%, rises by 10.1%, and drops by 11.5% for the Changbai Mountain, Inner Mongolia, and Northern China stations, respectively while the annual average of SHF rises by 10.6%, drops by 10.1%, and drops by 11.3% for the three areas.

Keywords sensible heat flux, latent heat flux, land use change, the Noah model

1 Introduction

Energy and water flux exchanges are the two most important processes at the interface between the land and the atmosphere. The land surface provides a continuous feedback to the atmosphere driven by the transfer of energy, which in turn drives the weather and climate systems (Meng et al., 2009). Accurate estimation of this feedback will help us to study atmosphere-land interactions and land surface and climate change processes. Hence, it is necessary and critical to accurately estimate the energy fluxes for studying climate change and for planning and managing water resources. Energy flux data of good quality at high spatial and temporal resolutions can help to improve the characterization of water and energy cycle (Xu et al., 2011).

The effective feedback from land surface into the atmosphere includes sensible heat flux (SHF) and latent heat flux (LHF), resulting from the partition of available energy at the land surface. The partition relates to a large combination of various factors (Zhang et al., 2009), including soil moisture content, soil temperature, various soil physical parameters, land use cover, albedo, air relative humidity, vegetation fraction cover, horizontal advection, biological properties of vegetation and soil, etc. (Pipunic et al., 2008). Due to the spatial heterogeneity of these factors, it is very challenging to accurately estimate the SHF and the LHF (Zhang et al., 2010).

Various methods and algorithms have been developed with regard to this problem. Currently, there are three common approaches to acquire the SHF and the LHF (Qin et al., 2009). The first approach is to take measurements in the field using the observation instruments. Field measurements have high spatial and temporal resolutions, yet are only representative at limited spatial scales. Since the SHF and the LHF have large spatial heterogeneity, it is not practical to densely deploy instruments in a large domain. The second approach is to retrieve the SHF and the LHF from remote sensing data. The retrieved results possess fine spatial resolutions and can cover large spatial domains, but are only representative instantaneously as the satellite passes over the area.

Received December 7, 2012; accepted June 14, 2013

E-mail: chensh@igsnrr.ac.cn

Land surface models (LSMs) provide the third approach (Meng et al., 2009; Qin et al., 2009), which have been developed over the past two decades (Dai et al., 2003). The LSMs simulate dynamic processes in the real world through physical equations and a combination of all the above mentioned factors in a mathematical framework. Driven by meteorological data and other parameters, LSMs estimate turbulent heat fluxes continuously at specific spatial and temporal scales. These models will likely prove to be the most efficient way to estimate the SHF and the LHF at a high temporal and spatial resolution. Among the LSMs, the Noah model is widely appreciated by the land surface research community because it applies a finite-difference spatial discretization method and a Crank-Nicholson time-integration scheme to numerically integrate the governing equations of the physical processes of the soil-vegetation-snowpack (Yang et al., 2011). Because of these advantages, the Noah model has been employed in this study. Detailed descriptions of the Noah formulations and development can be found in other literature (Chen and Dudhia, 2001; Sridhar et al., 2002; Sridhar et al., 2003; Yang et al., 2011).

Land use has a significant impact on the partition of net radiant energy (NRE), in conjunction with other closely related factors, such as physical, chemical, and biological properties (House-Peters and Chang, 2011). It is well known that the urbanization occurring in China is altering the landscape at an unprecedented rate (Deng et al., 2008). This form of land use change (LUC) can significantly reduce infiltration and runoff response times, in addition to altering the daily trends of energy and water vapor fluxes. Many studies have shown that the change in water and energy fluxes at the interface between the land and atmosphere is mainly caused by LUC which in turn is responsible for unwanted disasters and extreme weather (Kishtawal et al., 2009; Zhang et al., 2009; Yang et al., 2010). Hence, it is urgent to study the relationship between the NRE partition and LUC by modeling the water and energy fluxes in order to safeguard future ecological security.

Understanding the impact of LUC on the partition of the NRE is particularly important to enhance the adaptive capacity of an arid or semi-arid region which is subject to water resource scarcity. The Noah model (Mahrt and Ek, 1984) is used in this study to estimate the response of the NRE partition to future (2015–2034) land use patterns. The simulation results of the SHF and LHF between 2003 and 2005 were validated using the observation data from the Changbai Mountain, Xilinhot, and Yucheng stations. The simulation results from 2015 and 2034 are used to project the evolving trend of the SHF and LHF.

The main objective of this paper is to understand the role of LUC on the regional energy cycle. The specific research question addressed is: what is the impact of LUC on land surface energy fluxes? Projected future land use maps are used to identify the role of LUC.

2 Methodology and data

2.1 The Noah model

The initial Noah model, developed by Pan and Mahrt (1987), was based on the Penman potential evaporation approach, the multi-layer soil model, and the primitive canopy model. Later, the Hydrology Office of National Centers for Environmental Prediction (NCEP) and the Office of Research and Applications of National Environmental Satellite, Data and Information Service (NESDIS), expanded a series of improvements to optimize the Noah for use in operational weather and climate prediction models.

The Noah included a physically based parameterization of frozen soil (Sridhar et al., 2003) and used a finite-difference spatial discretization method and a Crank-Nicholson time integration scheme (Yang et al., 2011). State variables included skin temperature, soil moisture and temperature in four soil layers, canopy intercepted water, and ground accumulated snow, etc.

The energy balance in the Noah is formulated as:

$$R_n = G + H + \lambda E. \tag{1}$$

In Eq. (1), R_n is the NRE, and is split into LHF (λE), SHF (H), and ground heat flux (GHF) (G). These flux components are computed using physically-based equations. Four-level soil layer configuration with thicknesses of 0.1, 0.3, 0.6, and 1.0 m is adopted in the Noah for catching the daily, weekly, seasonal, and yearly changes in soil moisture. The Noah can accommodate one canopy layer. Skin temperature is determined according to a linearized energy balance equation that can characterize the combined ground and vegetation surface (Niu et al., 2011).

In the Noah model, the LHF is the sum of soil evaporation (E_s), canopy evaporation (E_c), and vegetation transpiration (E_t) in $\text{kg}\cdot\text{m}^{-2}\cdot\text{s}^{-1}$. The E_s, E_c, and E_t are then calculated, using potential evapotranspiration (E_p) in $\text{kg}\cdot\text{m}^{-2}\cdot\text{s}^{-1}$ according to Eqs. (2), (3) and (4) (Mahrt and Ek, 1984):

$$E_s = (1-f)\beta^b E_p, \tag{2}$$

$$E_c = fE_p\gamma^n, \tag{3}$$

$$E_t = fE_pB_c(1-\gamma^n), \tag{4}$$

where E_p is the potential evapotranspiration which can be obtained using the Penman equation (Mahrt and Ek, 1984), f is vegetation fraction coverage (%), β is relative soil volumetric water content (%), b is the empirical coefficient (1–2), γ is water canopy interception percent (%), n is constant and always evaluated with 0.5, and B_c is the function of canopy resistance.

The GHF is obtained using skin temperature (T_s) and the first layer soil temperature (T_1) as (Peters-Lidard et al., 1997):

$$G = K\frac{T_s - T_1}{0.5z_1}. \tag{5}$$

In Eq. (5), K is the soil heat conductivity ($\mathrm{W \cdot m^{-1} \cdot K^{-1}}$) and z_1 is the first layer soil thickness.

The SHF is derived as:

$$H = \rho c_p C_h u(\theta_s - \theta_{air}). \tag{6}$$

In Eq. (6), θ_s is the skin potential temperature (K), θ_{air} is the air temperature (K), ρ is the air density ($\mathrm{g \cdot cm^{-3}}$), c_p is the specific heat of dry air at constant pressure, u is the wind speed ($\mathrm{m \cdot s^{-1}}$), and C_h is the exchange coefficient between heat and water vapor on the ground.

The Noah model requires two types of input data: soil and vegetation parameters and meteorological forcing data. Both types of data are discussed in the following two sections.

2.2 Land use, soil and vegetation data

Four future scenarios (2015, 2020, 2025, and 2030) of LUC are used in this study. These data are provided by the Center for Chinese Agricultural Policy (CCAP), Chinese Academy of Sciences (CAS). The reference data used to produce the four projected LUC scenarios are the Landsat Thematic Mapper and enhanced Landsat Thematic Mapper digital images (Deng et al., 2006).

The spatially explicit data of the LUC scenarios for the four periods are produced using the dyna-CLUE model (Verburg and Overmars, 2009). The Dyna-CLUE combines the top down allocation of land use change to grid cells with a bottom-up determination of conversions for specific land use transitions. The analysis starts by grouping the land use types into two groups: those driven by demand at the regional level and those for which no aggregate demand at the regional level can be determined. This dyna-CLUE model integrates demand-driven changes in the land area with locally determined conversion processes in a large scale, top-down, modeling framework, enhanced to incorporate dynamic land cover, economics, and policy, and allows a balanced and integrated analysis of varying types of dynamics at the cost of requiring a simplification of the local processes. The combination of top-down and bottom-up processes within a single allocation model can better address the cross-scale interactions in land use modeling (Verburg and Overmars, 2009).

Projected LUC scenarios are aggregated using a majority filter (the value that appears most often) in order to match the spatial resolution of the Noah, and are converted to the geographic projection with the unit of the latitude and longitude coordinates in degree. If no majority value exists, the neighborhood parameters could be altered to include more grid cells. The four LUC scenarios are reclassified into the land use types (Table 1) used in the Noah.

In the Noah model, the soils are divided into nine types, shown in Table 2. The soil data are derived from the global soil distribution data provided by the Food and Agricultural Organization of the United Nations according to the Zobler classification standard (Zobler, 1986). This classification standard determines the soil type according to the content proportion of the clay, silt, and sand contained in the soil (Reynolds et al., 1999).

Predetermined vegetation parameters include roughness, minimum stomatal resistance, etc. Predetermined soil parameters include the depths of the four soil layers, maximum soil volumetric water content, saturated soil moisture diffusivity, wilting coefficient, and the quartz content of the soil. Both data are adapted from the datasets published by the Global Soil Wet-ness Project (GSWP) (Dirmeyer, 2011).

Quarterly averaged snow-free ground albedo and monthly averaged vegetation fraction cover data are provided by the climate and vegetation research group of Boston University, and retrieved, respectively, from Moderate Resolution Imaging Spectroradiometer (MODIS) and Advanced Very High Resolution Radiometer (AVHRR) data with a 1 km resolution. Leaf Area Index (LAI) and stem area index are produced from the MODIS products.

The elevation is derived from the 1 km digital elevation

Table 1 The land cover classes used in the Noah model

Class code	Land cover	Class code	Land cover
1	Evergreen needle-leaf forest	8	Closed shrub-land
2	Evergreen broad-leaf forest	9	Open shrub-land
3	Deciduous needle-leaf forest	10	Grassland
4	Deciduous broad-leaf forest	11	Cropland
5	Mixed cover	12	Bare ground
6	Woodland	13	Urban and build-up
7	Wooded grassland		

Table 2 The soil classes used in the Noah model

Type code	Name	Type code	Name
1	Loamy sand	6	Clay loam
2	Silty clay loam	7	Sandy clay loam
3	Light clay	8	Organic
4	Sandy loam	9	Loamy sand
5	Sandy clay		

of the GTOPO30 database (Verdin and Greenlee, 1996). The vegetation classification is derived from the global, 1 km, AVHRR based, 13 class vegetation database. The 9-class soil texture data are derived from the top layer of the 1 km, 11-layer soil dataset, state soil geographic database (Miller and White, 1998).

2.3 Meteorological forcing data

Princeton meteorological forcing data from 2003 to 2005 are used for historical climate forcing. The meteorological variables include air temperature (K), wind speed ($m \cdot s^{-1}$), pressure (Pa), specific humidity ($kg \cdot kg^{-1}$), precipitation ($kg \cdot m^{-2} \cdot s^{-1}$), solar shortwave radiation ($W \cdot m^{-2}$), and downward longwave radiation ($W \cdot m^{-2}$). The Princeton forcing data have a spatial resolution of $1° \times 1°$ and a temporal resolution of 3 hours.

For the purpose of this study, which primarily focuses on the responses of the LHF and the SHF to LUC, we use Princeton Meteorological forcing data to determine future climate forcing. The main purpose of this paper is to discuss the effect of LUC on the partition of the NRE, hence stationary meteorological conditions are considered. The forcing data from 2000 to 2004 are used repeatedly to simulate the meteorological condition from 2015 to 2034 to minimize the changes of the heat and water fluxes caused by the climatic change.

2.4 The validation data and the study area

The Chinese Ecosystem Research Network (CERN) was established in 1988 for ecological studies. The network provides continuous ecosystem observations for the study of biogeochemical, water, energy, and momentum processes at diurnal to annual scales. The network is currently comprised of 46 stations distributed across the entire country. The validation data used are in situ observations from the Changbai Mountain, Xilinhot, and Yucheng stations. These three stations represent the forest ecosystem, grassland ecosystem, and farmland ecosystem, respectively, and are geographically located at (42.40° N, 127.09° E), (43.50° N, 117. 45° E) and (36.96° N, 116.63° E). Figure 1 shows the schematic locations of the three stations.

The SHF and LHF have been continuously measured at all three stations by the eddy correlation system, which is composed of a 3D sonic anemometer and an open path CO_2/H_2O analyzer. The validation data were obtained by averaging the original data of 10 Hz over a 30 minute window. The temporal span for the available data is from April to July between 2003 and 2005.

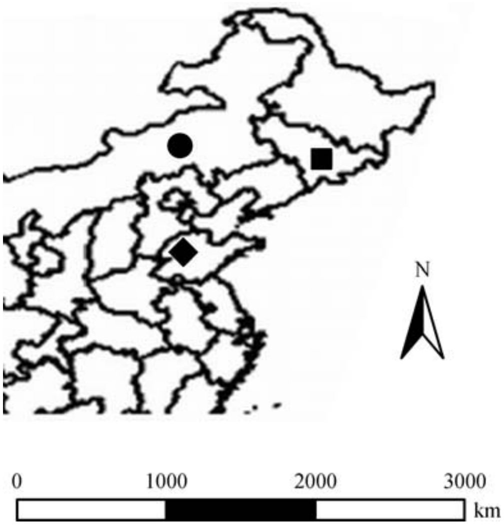

Fig. 1 The schematic locations of the Changbai Mountain Station (■), the Xilinhot Station (●), the Yucheng Station (◆).

The climate for the region around the Yucheng Station is the continental monsoon of warm temperate zone. Over the past 30 years, yearly averages were shown for temperature at 13.1°C, precipitation at 600 mm, solar radiation at 5,225 $MJ \cdot m^{-2}$, and relative humidity at 66.44%. The soil is mainly classified as sandy-clay loam and sandy loam. The area around this station is characteristically agricultural with wheat and corn alternately cultivated.

The Xilinhot Station lies in the Xilin river basin of Inner Mongolia. This area belongs to a continental semi-arid climate. Approximated yearly averages are shown for temperature as 1.5°C, precipitation as 400 mm, and evaporation as 1,665 mm The average canopy height is 50–60 cm, vegetation coverage is greater than 80%, and grass becomes green in April and wilts in October (Chen et al., 2009).

The climate for the Changbai Mountain area in East Asia is temperate continental monsoon. Average annual temperature is between −7°C and −3°C, precipitation between 700–1,400 mm, and evaporation between 1,200–1,500 mm.

The underlying footprints of the three stations are relatively homogeneous and cover the spatial domain by approximately 1.5 km × 1.5 km. Therefore, the observation data can represent the water and energy exchange status of the homogeneous areas around these stations. The three areas correspond to at least one grid of the Noah model when it is run at the spatial resolution of 0.01° × 0.01°. It is not sufficient to use these observation data as validation data between April and July from 2003 to 2005. However, there is no observation data available at the same scale of tens of kilometers.

3 Results and discussion

3.1 The validation of the Noah simulation

The performance of the Noah model for simulation of energy and water flux exchanges at the spatial resolution of 0.01°×0.01° is quantitatively estimated using the correlation coefficient (CC) and the relative error (RE) (i.e., a percentage of the difference between the Noah simulation and the observation to the observation) at the three stations. Ideally, CC and RE should be close to 1 and 0.

To match the three hour resolution of the Noah results, the observation data at 30 minutes intervals are averaged to one per three hours. Both the Noah results and the observation data at a three hours resolution are then averaged to derive the monthly diurnal curve. Tables 3 and 4 show the CC and the RE results respectively for the monthly diurnal LHF and the monthly diurnal SHF between April and July from 2003 to 2005. Because the observation data for the Xilinhot Station in 2003 are not available, the CC and the RE for 2003 cannot be calculated. Hence, the corresponding columns in Tables 3 and 4 are blank.

It can be seen from Tables 3 and 4 that both the CC and the RE show good performance for the SHF and the LHF at the three stations. From these evaluation results, we can conclude that the Noah predictions of θ_s, E_s, E_c, and E_t can be trusted as reliable given that SHF is dependent on θ_s according to Eq. (6) while the LHF is the sum of E_s, E_c, and E_t. This implies that the Noah model is capable of capturing the monthly diurnal patterns of the water and energy exchange with the Princeton forcing and land surface parameter data.

As shown in Tables 3 and 4 CC and RE do not yet reach the ideal values of 1 and 0, respectively. This is due to the uncertainty in the land surface parameters, which are mainly determined by soil type and soil texture map with a finite accuracy, and also to the low spatial resolution of the precipitation data of the Princeton forcing. As for the LHF and the SHF, the influencing factors include the uncertainties of soil and vegetation property data, the assumptions, and the empirical equations used in the Noah model.

In order to facilitate the validation, the monthly diurnal cycles from both the Noah results and the observation data are displayed in the following figures. Figures 2 and 3 show the intercomparison of the LHF and the SHF respectively. For the LHF, it can be seen from Fig. 2(a) that the Noah results are lower than the observation data for the Yucheng Station except during the final month in the series. Figure 2(b) shows that the Noah results are higher than the observation data for the Changbai Mountain Station. From Fig. 2(c), we can see that the Noah results agree very well with the observation data for the Xilinhot Station. For the SHF, Fig. 3 shows that the Noah result is higher than the observation data for the three stations.

In order to comprehensively evaluate the performance of the Noah model, both the Noah results and the observation data of monthly diurnal are averaged to monthly. CC and RE are calculated using the Noah results, and the observation data of monthly resolution between April and July from 2003 to 2005. Table 5 shows the results.

Table 5 shows that the monthly averages of the Noah

Table 3 The CC results of the monthly diurnal LHF and SHF

Station	2003		2004		2005	
	LHF	SHF	LHF	SHF	LHF	SHF
Yucheng	0.8126	0.8516	0.8192	0.8941	0.8094	0.8764
Changbai	0.8896	0.8777	0.9052	0.9163	0.8954	0.9051
Xilinhot			0.9153	0.8644	0.8827	0.9194

Table 4 The RE results of the monthly diurnal LHF and SHF (%)

Station	2003		2004		2005	
	LHF	SHF	LHF	SHF	LHF	SHF
Yucheng	6.67	11.8	23	24.6	13.8	12.7
Changbai	11.03	16.5	20.6	33.6	23.4	33.3
Xilinhot			15.5	14.1	9.8	21.6

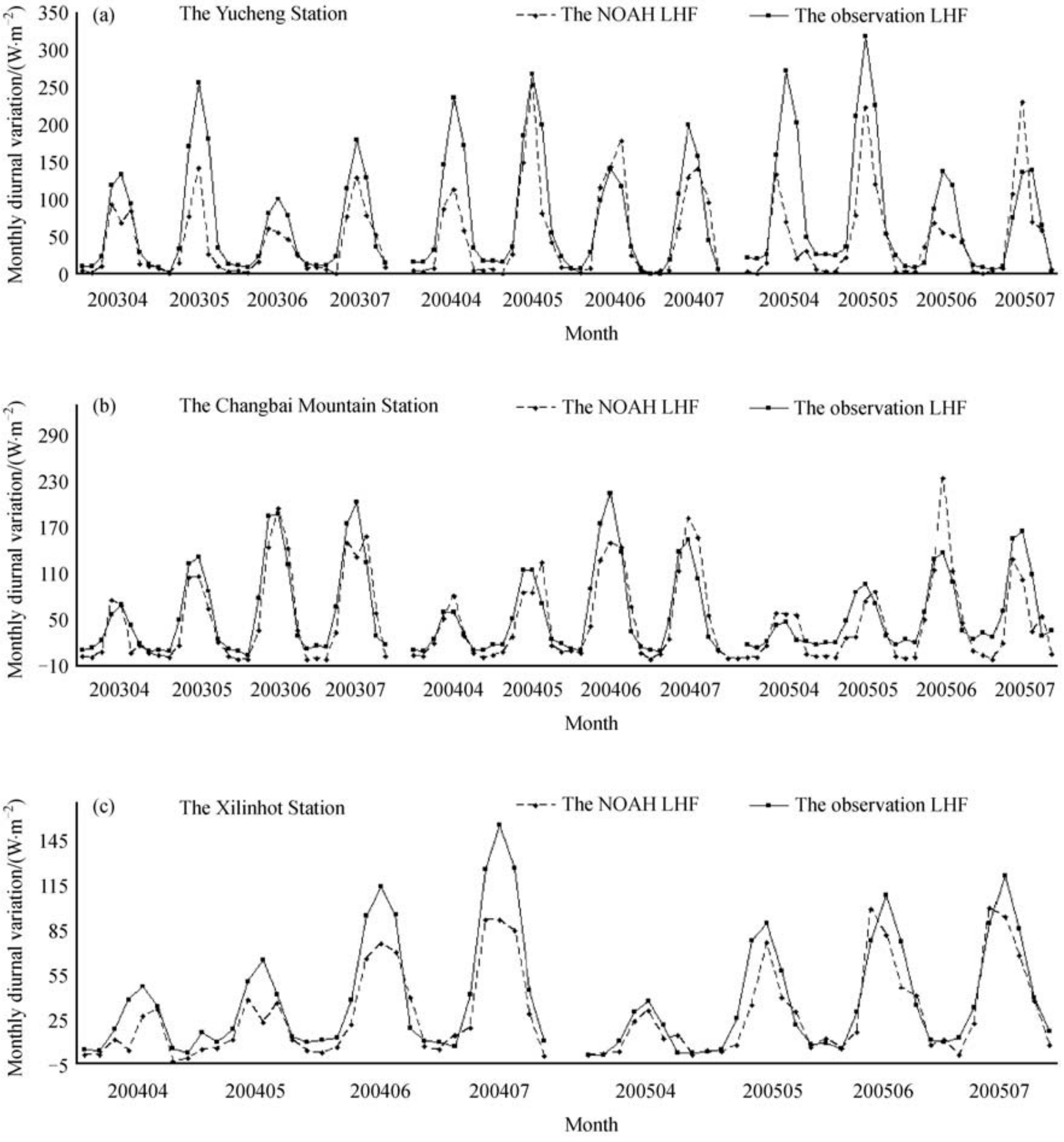

Fig. 2 Monthly diurnal variation of the LHF for the Yucheng Station (a), the Changbai Mountain Station (b) and the Xilinhot Station (c).

model match the in situ observation data well according to the CC and the RE. It indicates that the performance of the Noah appears to be robust and reliable, and the monthly simulation results are able to characterize the change process of the water and heat exchange over the three stations. Compared with the observation data of the LHF and the SHF, we can see that the Noah model provides a reliable simulation of the energy budget. Table 5 reveals that the Noah model can give satisfactory results. It is also consistent with the conclusion drawn from Tables 3 and 4.

Overall, the Noah model simulates the energy and water fluxes well, because the Noah has a sound parameterization by taking into account the separation of topsoil, snow, and vegetation canopy, as is the case of the multi-layer soil model and the primitive canopy model (Pan and Mahrt, 1987), sub-grid scale heterogeneity, as is the case of the diurnally dependent Penman potential evaporation approach (Mahrt and Ek, 1984). These special features make it possible for the Noah model to produce predictions close to the observation data.

3.2 The Noah prediction in different climate scenarios

For each region around the three stations, one rectangle block with a span of 8 × 8 cells, at the spatial resolution of 0.25° × 0.25°, is selected. The Noah model is configured

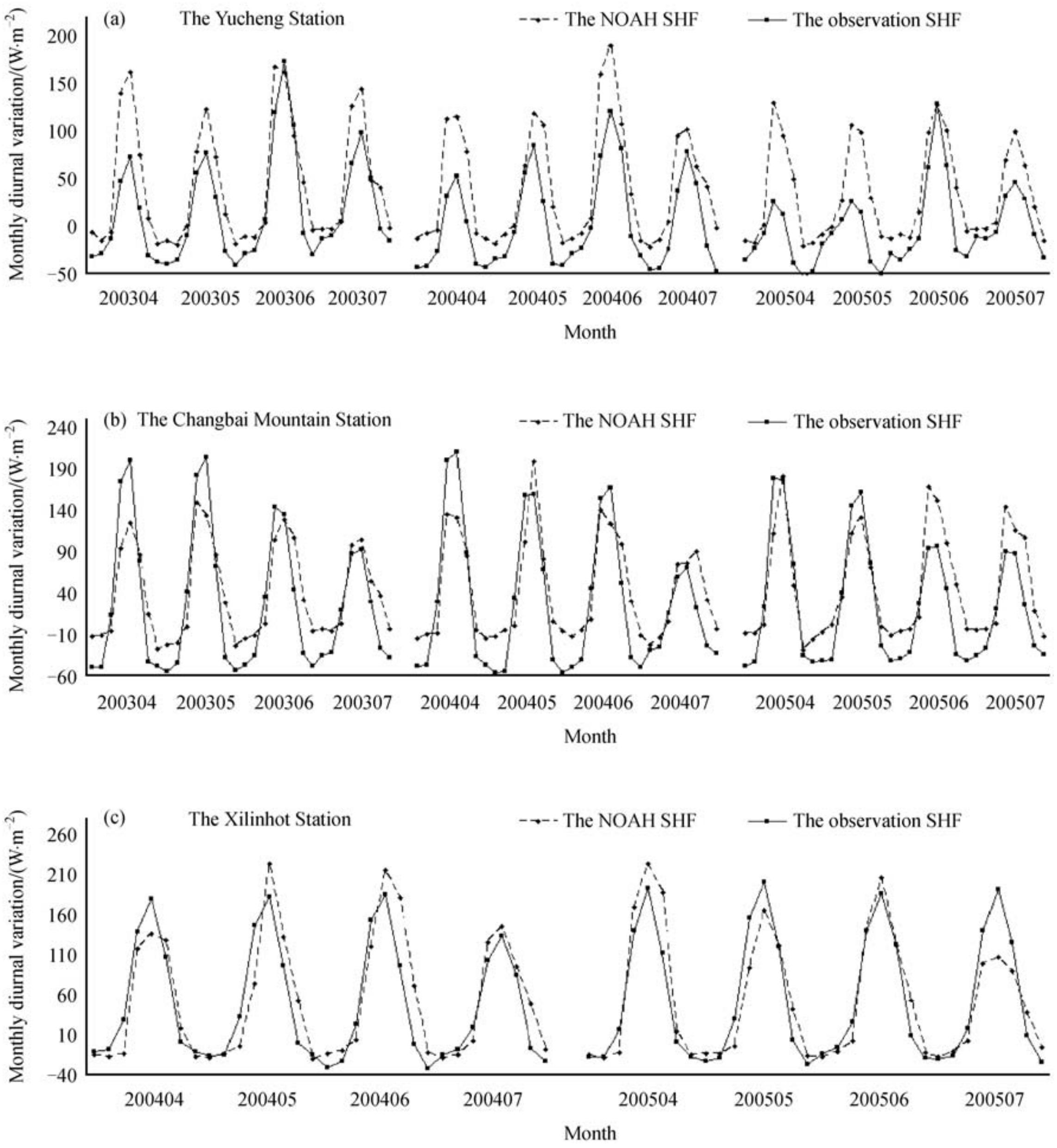

Fig. 3 Monthly diurnal variation of the SHF for the Yucheng Station (a), the Changbai Mountain Station (b) and the Xilinhot Station (c).

Table 5 The CC and RE results of the monthly LHF and SHF

Station name		Yucheng	Changbai	Xilinhot
CC	LHF	0.8563	0.9324	0.9507
	SHF	0.9192	0.9281	0.9484
RE/%	LHF	15.36	15.98	11.23
	SHF	17.21	25.95	14.38

to a 3 hour resolution, with a temporal span between 2015 and 2034. Figure 4 shows the spatial distribution of the land use for the areas surrounding the three stations during the five-year periods of 2015, 2020, 2025, and 2030. Tables 6–8 display the percentage of change for each of the 13 land use classes in the areas surrounding the three stations.

Due to the rapid economic development occurring in

Table 6 The percentage of change for the 13 land use classes in the region surrounding the Changbai Mountain Station

Land cover	2015	2020	2025	2030
Evergreen needle-leaf forest	0.3789	0.3767	0.3444	0.2922
Evergreen broad-leaf forest	1.1467	1.0233	0.6089	0.5933
Deciduous needle-leaf forest	1.4244	1.3133	1.8167	1.8922
Deciduous broad-leaf forest	5.9656	4.5644	4.0411	4.1133
Mixed cover	2.1744	4.4944	4.9822	4.8789
Woodland	14.53	12.4478	14.4233	13.7678
Wooded grassland	8.9567	7.41	3.7033	3.8267
Closed shrub-land	3.4056	9.4478	12.0133	11.5278
Open shrub-land	9.88	8.8067	5.2156	5.4711
Grassland	4.2233	7.6789	4.77	5.0378
Cropland	42.0056	37.08	38.6556	38.9867
Bare ground	4.0911	4.3256	7.5833	7.67
Urban and build-up	0.8411	0.4156	0.8644	0.96

Table 7 The percentage of change for the 13 land use classes in the region surrounding the Xilinhot Station

Land cover	2015	2020	2025	2030
Evergreen needle-leaf forest	0.2633	0.1856	0.2611	0.2411
Evergreen broad-leaf forest	0.5322	0.3289	0.0956	0.1011
Deciduous needle-leaf forest	0.9489	0.6944	0.9667	0.9578
Deciduous broad-leaf forest	0.9122	0.6411	0.26	0.2722
Mixed cover	0.8089	1.82	2.5178	2.3611
Woodland	5.2589	4.1522	5.0311	5.0411
Wooded grassland	5.7844	5.08	2.7256	3.0522
Closed shrub-land	4.8778	8.1033	9.1833	10.4067
Open shrub-land	10.89	13.5856	8.4144	7.9033
Grassland	54.32	52.4156	52.2733	51.9878
Cropland	11.95	11.29	14.7922	14.5311
Bare ground	3.0656	1.4378	3.0867	2.7089
Urban and build-up	0.0833	0.0322	0.0867	0.0867

China, the ecological environment is experiencing global degradation as well as local improvement. The governance capacity lags behind the destruction speed, and the ecological deficit is gradually increasing. The reality of these conditions is primarily reflected by a decrease in forest resources, aggravated grassland degeneration, and a decline in groundwater levels. Studies of these three representative areas, based on the future projections of LSMs, had never previously been reported.

The decrease in forest resources drop has become more and more aggravated (Deng et al., 2010). This condition is especially critical in the Changbai Mountain region, which is the main forest region of China. The deforestation rate of this region outpaced the rate of forest reserves. According to the current consumption speed, the resources provided by mature forests to most national forest enterprises will soon be depleted (Deng et al., 2010). The ongoing abuse of these resources by the current generation will sacrifice any potential benefit for future generations. This area is shown in Fig. 4(a). The main purpose of the Changbai Mountain Station is to monitor the climate change of this region (Liu et al, 2005).

In the 1970s, the degeneration rate of the grassland area is 8.25%. It is above 25% in the mid-1980s for China (Rozelle et al., 1997). The grassland degeneration area has reached up to 100 million hectares. There are currently more than one million hectares per year for degeneration. The production of natural grasslands consistently falls with large areas of grassland degeneration. The most severe region is Inner Mongolia, indicated in Fig. 4(b). The

Table 8 The percentage of change in the 13 land use classes in the region surrounding the Yucheng Station

Land cover	2015	2020	2025	2030
Evergreen needle-leaf forest	0.18	0.0656	0.18	0.0722
Evergreen broad-leaf forest	0.2133	0.2489	0.0067	0.0011
Deciduous needle-leaf forest	1.1689	0.2778	0.4711	0.3278
Deciduous broad-leaf forest	0.4433	0.3611	0.1322	0.1622
Mixed cover	0.0911	1.3933	2.4944	2.47
Woodland	2.6889	1.9589	2.54	1.8644
Wooded grassland	3.9711	3.5044	1.4822	2.4244
Closed shrub-land	3.6467	6.6244	5.9811	8.25
Open shrub-land	10.7811	13.2411	9.1078	10.4033
Grassland	25.2722	25.7989	25.9989	25.3967
Cropland	44.1467	38.5211	40.2444	36.8167
Bare ground	5.92	6.6367	9.8067	10.1744
Urban and build-up	1.1533	1.1933	1.2222	1.3633

Xilinhot Station was established in this region to monitor the impact of climate change on grassland degeneration (Chen et al., 2009).

During the past several years, the excessive exploitation of ground water produced an underground funnel of over fifteen thousand km^2 in northern China (Cao et al., 2009), which resulted in a decline of 12 cm per year in the groundwater level. Currently, groundwater is the main source for agriculture and residential use in this region. Predicting the water exchange between the land surface and the atmosphere is urgent to aggressively monitor the ground water level. This region is shown in Fig. 4(c). One purpose of the Yucheng Station is to monitor the environmental and ecological changes caused by ground water decline (Zhang et al., 2008).

By using the four projected LUCs, both the monthly and yearly averages of the LHF and the SHF for the three regions are respectively shown in Figs. 5–7.

Figure 5 shows that monthly average variations of the LHF and the SHF exhibit approximate sinusoidal curves. The annual average values of the LHF and the SHF between 2015 and 2034 fluctuate from 50 to 100 W/m^2. From the standpoint of a broad comparison, the averages are approximately 70 W/m^2 higher between 2015 and 2034 than those from 2003 to 2005 (see Figs. 2(b) and 3(b)). It is therefore determined that the net radiation consumed for the LHF and the SHF increases when the LUC is transformed from forest to planting or bare land in this region.

As seen in Fig. 5, the slopes for the annual LHF and SHF are -0.1076 and 0.1059 respectively, which indicates that the annual LHF has a slightly downward trend while the SHF continues to increase. The phenomena can be explained by carefully examining Fig. 4(a) and Table 6; it is found that the forest area in the Changbai Mountain region gradually decreases from 2015 to 2034. With the continuous development of the forestry market, combined with decreasing agricultural activities in Northeast China, which is one of the assumptions used to produce the projected land use maps using the Dyna-CLUE model, the high percentage of deforestation indicates that larger areas can be classified as a land use of either ‘recently abandoned,’ ‘semi-natural,’ or ‘planting seedling,’ from 2015 to 2034.

It can be seen from Fig. 6 that the monthly average of the LHF and SHF in the Inner Mongolia grassland, show approximate seasonal periodicity. The changes of the LHF and SHF can be analyzed based on the general comparison of the change in LUC since the Xilinhot Station was built . Using Figs. 2(c) and 3(c) as references, the multi-year average values of the LHF and the SHF respectively changed from 40 and 80 W/m^2 between 2003 and 2005 to 40 and 100 W/m^2 between 2015 and 2034.

Fig. 6 shows that the slopes for the LHF and the SHF are 0.1018 and -0.1019, respectively, which means that the LHF has a upward trend while the SHF has a downward trend. From Fig. 4(b) and Table 7, we can see that the grassland area in Inner Mongolia gradually decreases because a large part of it gradually changes to mixed land. This land conversion is attributed to overgrazing. When producing the projected land use maps using the Dyna-CLUE model, it is assumed that more cattle and sheep are fed on grass, which leads to the conversion of infertile grassland to bare soil (see Fig. 4(b)). Table 7 indicates the percentage of each type of land use in the four future scenarios. In some areas, the protected grassland may have been exploited by increasing the grazing area at locations not previously used for animal husbandry. The spatial pattern clearly shows that the grassland degeneration is mainly found in regions that are being developed for the industry to livestock.

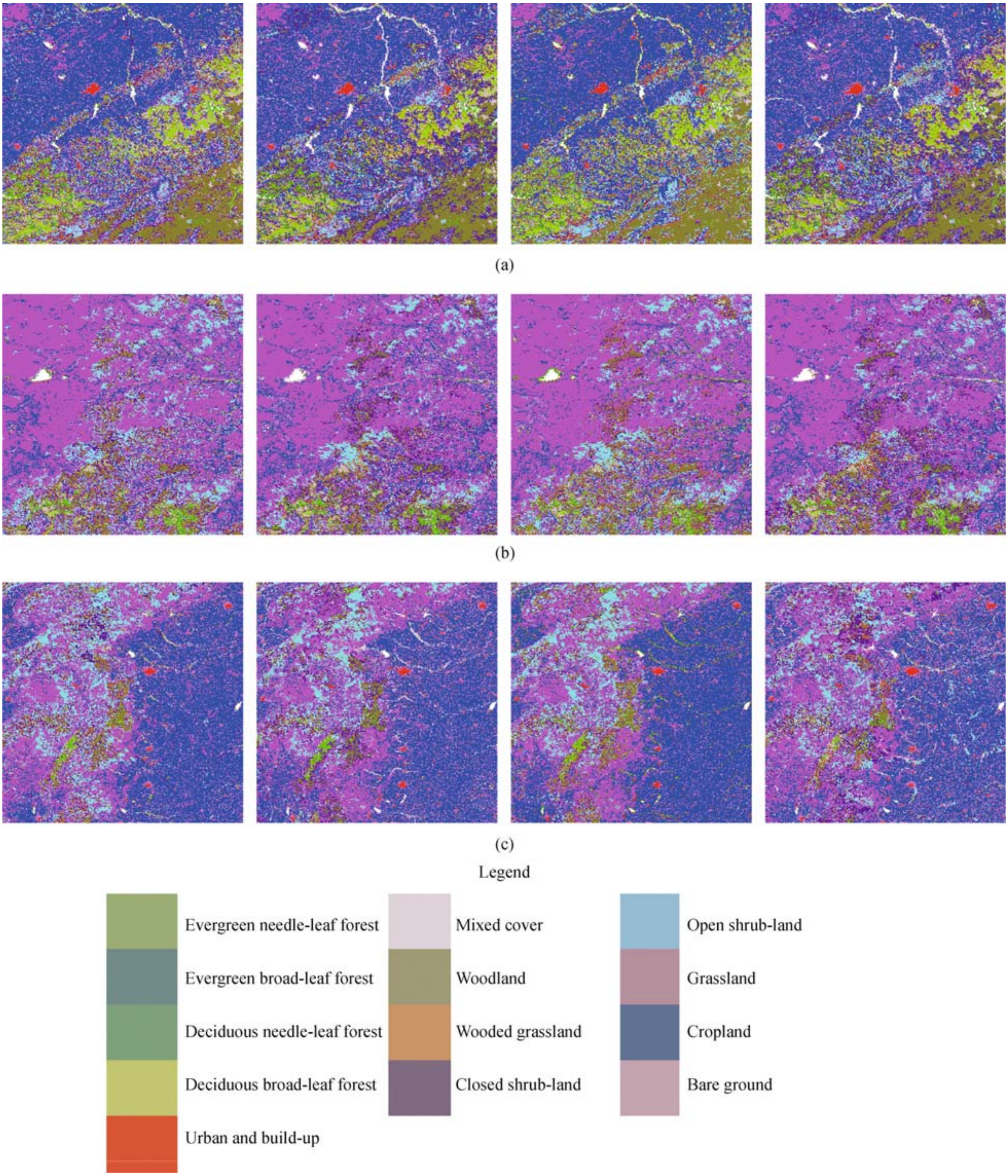

Fig. 4 The land use maps for 2015, 2020, 2025, and 2030 for the three stations.

Figure 7 shows the variation of the LHF and the SHF for northern China. Overall, the multi-year average values of both the LHF and SHF, from 2015 to 2034 respectively (Figs. 7(a) and 7(b)), are approximately equal to 50 W/m^2. The slopes for the LHF and SHF are -0.115 and 0.1126. That means that the LHF would decrease in the long term, while the SHF seems to have an increasing trend. The northern China region is primarily agricultural, and irrigation water is generally extracted from the groundwater. The LHF mainly comes from the crop transpiration (Zhang et al., 2008). If we continue to rely on ground water resources to support the agriculture in this region, one

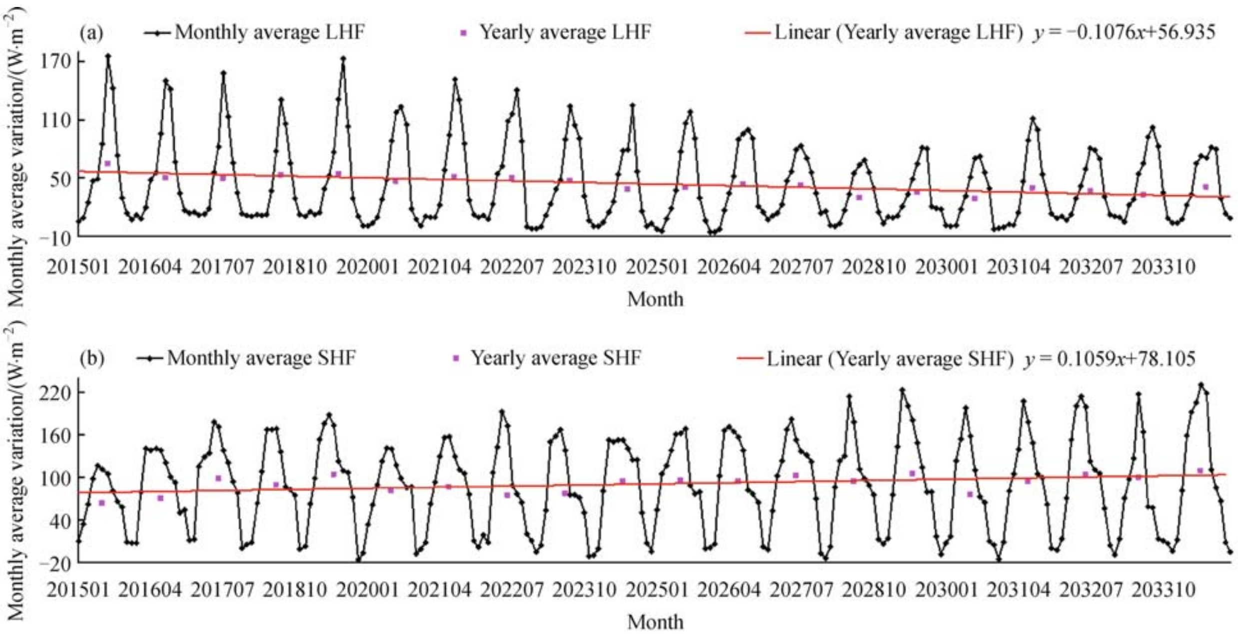

Fig. 5 Monthly average variations of the LHF (a) and the SHF (b) for the Changbai Mountain.

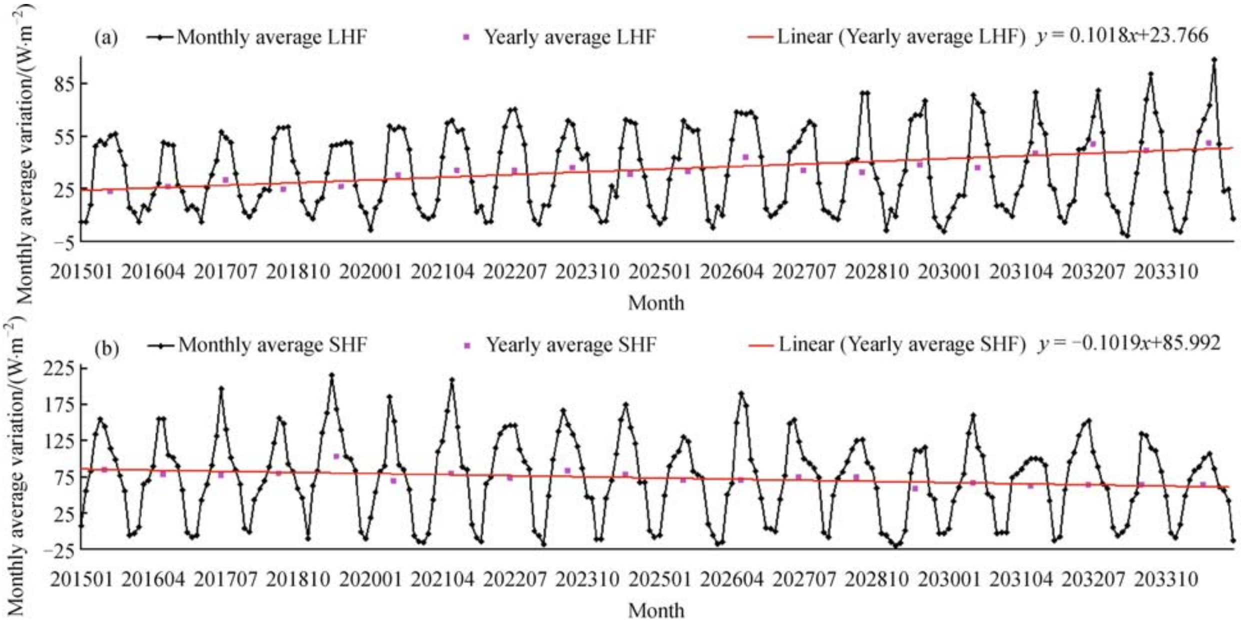

Fig. 6 Monthly average changes of the LHF (a) and the SHF (b) for Inner Mongolia.

consequence is that more groundwater will be evaporated into the atmosphere.

It can be found in Fig. 4(c) and Table 8 that mixed uses gradually increase, and a small fraction of cropland is transformed to urban. During the production of the projected land use maps using the Dyna-CLUE model, it is assumed that the urban area would have to expand due to the urbanization from 2015 to 2034.

As shown in Figs. 5(a), 6(a), and 7(a), LHF reaches the maximum value in June or July every year. The monthly average LHF value for the Changbai Mountain is the highest among the three regions, and is the lowest for Inner Mongolia. The reason behind these phenomena is that the LAI and the vegetation type are major factors controlling the proportion of the transpiration to the net radiation. Generally speaking, the greater the LAI, the greater the

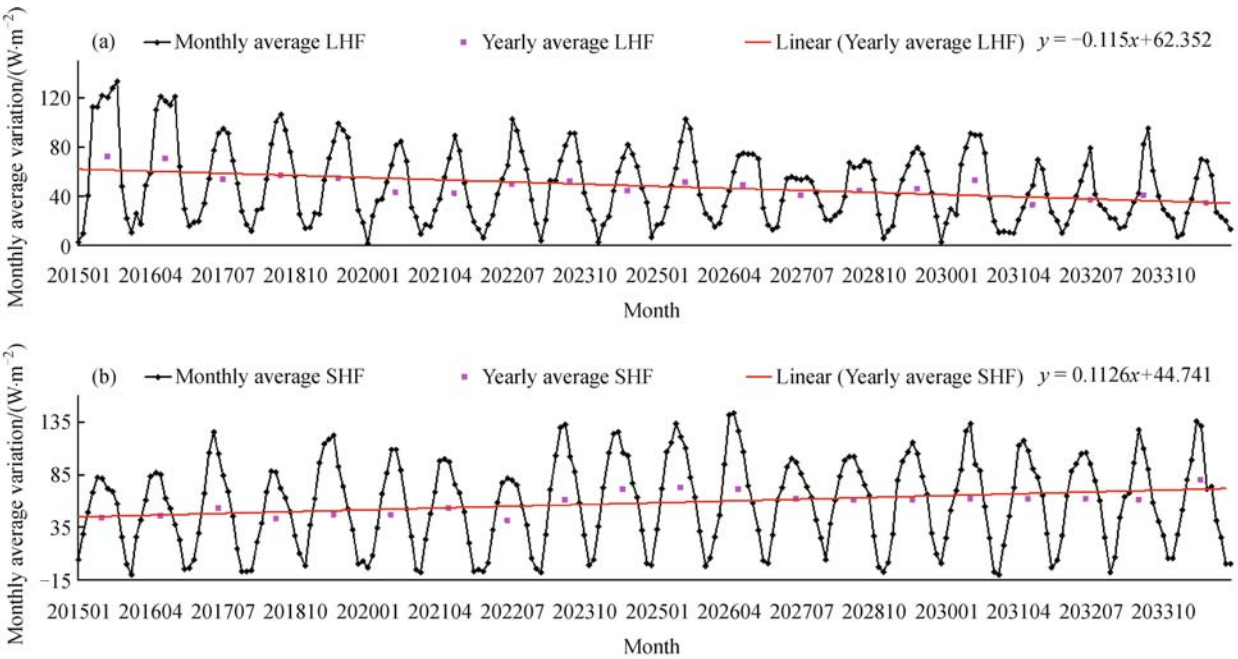

Fig. 7 Monthly average changes of the LHF (a) and the SHF (b) for northern China.

average value of the LHF. The order of the LAI values for the three regions from highest to lowest is Changbai Mountain, northern China, and Inner Mongolia, which is consistent with the order of the average values of the LHF for the three regions.

From Figs. 5(b), 6(b), and 7(b), it can be found that the SHF shows an obvious seasonal cycle and attains the maximum value in summer every year. The monthly average values of the SHF for the Changbai Mountain and Inner Mongolia are almost equal, and for northern China it is lower. In the Changbai Mountain, the forest covered land is changed to mixed or idle land use due to deforestation, while the overgrazing in Inner Mongolia leads to the conversion of the grassland to naked soil. The characteristics of the location and the LUC are the main reason for the difference of SHF. It is clear that the land use of northern China has a lower succession speed as compared to the succession in the other two areas. Geographic latitude is probably another reason. The geographic latitudes of the Changbai Mountain and Inner Mongolia are nearly equivalent, and are much higher than those of northern China.

The Noah predictions made using the projected LUCs from 2015 to 2034 provide 20 years of energy and water flux exchange over the areas of deforestation, grassland degeneration area, and northern China. Based on these results, the magnitude and the trends of future energy and water change can be investigated for the three environmentally fragile areas. It can be seen from these results that the partition of the net radiation into the LHF and the SHF is directly dependent on land use. The trends of the LHF and SHF reveal the consequent impact of different LUC scenarios on energy and water exchange between the Earth's surface and the atmosphere.

Because both the LUC and the forcing can affect the energy fluxes, it is difficult to discern the respective contributions if both aspects are simultaneously considered. In this paper, the trends of land surface energy fluxes under different LUCs and the same forcing are studied. Future study will focus on the effect of the forcing on land surface energy fluxes. When the LUC is unchanged, the effect of the forcing can be evaluated using different forcing. Additionally, the individual trend for each month is also important, which should be studied systematically. Because these are not directly related to the purpose of this paper, they will be discussed in subsequent papers.

4 Summary and conclusions

In this paper, four periods of land use scenarios (2015, 2020, 2025, and 2030), together with the forcing data from Princeton, are employed to drive the Noah model. The trend of the response of SHF and LHF to the LUC over three typical ecological zones in China is originally quantified using the Noah results for foreknowing the partition status of the NRE in land-atmosphere interaction.

The simulation results of the SHF and the LHF are validated using the observations from three field stations. The validation results show that the Noah performs reasonably well to simulate the heterogeneous and homogeneous land surface processes at large scales. For future scenarios, three new findings about the energy partition can be drawn: 1) the LHF has a reducing trend and the SHF seems to increase due to deforestation for the Changbai Mountain; 2) for Inner Mongolia, the LHF increases and the SHF decreases from 2015 to 2034 with grassland degeneration; 3) the LHF and the SHF have downward and upward trends over the long term because of over exploitation of groundwater and the urbanization expansion in northern China. In addition to supporting the argument that the LUC has a determinant impact on the partition of the surface energy balance components, this investigation quantitatively shows the possible variation in the LHF and the SHF that can result from future land use conversion. These conclusions are of importance in understanding the functionality of land uses in land-atmosphere exchange processes and for forecasting the potential risks caused by ecological disturbance.

Acknowledgements The authors thank the anonymous reviewers for their sincere suggestions which helped to improve the paper, and thank the CERN flux network for providing the validation data used in this paper. This work is supported jointly by National Basic Research Program of China (Nos. 2010CB950904 and 2010CB428403), the Project of National Natural Science Foundation of China (Grant Nos. 41101329 and 41371348).

References

Cao J, Cheng X, Li X (2009). Groundwater use and its management: policy and institutional options in rural areas of North China. Groundwater Governance in the Indo-Gangetic and Yellow River Basins: Realities and Challenges, 201–220

Chen F, Dudhia J (2001). Coupling an advanced land-surface/hydrology model with the Penn State-NCAR MM5 modeling system. Part I. Model implementation and sensitivity. Mon Weather Rev, 129(4): 569–585

Chen S P, Chen J Q, Lin G H, Zhang W L, Miao H X, Wei L, Huang J H, Han X G (2009). Energy balance and partition in Inner Mongolia steppe ecosystems with different land use types. Agric Meteorol, 149 (11): 1800–1809

Dai Y J, Zeng X, Dickinson R E, Baker I, Bonan G B, Bosilovich M G, Denning A S, Dirmeyer P A, Houser P R, Niu G, Oleson K W, Schlosser C A, Yang Z L (2003). The common Land Model (CLM) version 1.0. Bull Am Meteorol Soc, 84(8): 1013–1023

Deng X Z, Huang J K, Rozelle S, Uchida E (2006). Cultivated land conversion and potential agricultural productivity in China. Land Use Policy, 23: 372–384

Deng X Z, Huang J K, Rozelle S, Uchida E (2008). Growth, population and industrialization and urban land expansion of China. J Urban Econ, 63(1): 96–115

Deng X Z, Jiang Q O, Zhan J Y, He S J, Lin Y Z (2010). Simulation on the dynamics of forest area changes in Northeast China. J Geogr Sci, 20(4): 495–509

Dirmeyer P A (2011). A history and review of the global soil wetness project (GSWP). J Hydrometeor, 12, 729–749.

House-Peters L A, Chang H (2011). Modeling the impact of land use and climate change on neighborhood-scale evaporation and nighttime cooling: a surface energy balance approach. Landsc Urban Plan, 103 (2): 139–155

Kishtawal C, Niyogi D, Tewari M, Pielke R A, Shepherd M (2009). Urbanization signature in the observed heavy rainfall climatology over India. International Journal of Climatology, doi: 10.1002/joc.2044

Liu J Y, Zhang Z X, Zhuang D F, Zhang S W, Li X B (2005). Research on the Temporally Change of Chinese Land Use Using Remote Sensing in 1990s (In Chinese). Beijing: Science Press

Mahrt L, Ek M (1984). The influence of atmospheric stability on potential evaporation. J Clim Appl Meteorol, 23(2): 222–234

Miller D A, White R A (1998). A conterminous United States multilayer soil characteristics dataset for regional climate and hydrology modeling. Earth Interactions, 2(2): 1–13.

Meng C L, Li Z L, Zhan X, Shi J C, Liu C Y (2009). Land surface temperature data assimilation and its impact on evapotranspiration estimates from the Common Land Model. Water Resour Res, 45(2): W02421

Niu G Y, Yang Z L, Mitchell K E, Chen F, Ek M B, Barlage M, Kumar A, Manning K, Niyogi D, Rosero E, Tewari M, Xia Y (2011). The community Noah land surface model with multiparameterization options (Noah-MP): 1. Model description and evaluation with local scale measurements. J Geophys Res, 116(D12): D12109

Pan H L, Mahrt L (1987). Interaction between soil hydrology and boundary layer developments. Boundary-Layer Meteorol, 38(1–2): 185–202

Peters-Lidard C D, Zion M S, Wood E F (1997). A soil-vegetation-atmosphere transfer scheme for modeling spatially variable water and energy balance processes. J Geophys Res, 102(D4): 4303–4324

Pipunic R C, Walker J P, Western A (2008). Assimilation of remotely sensed data for improved latent and sensible heat flux prediction: a comparative synthetic study. Remote Sens Environ, 112(4): 1295–1305

Qin J, Liang S L, Yang K, Kaihotsu I, Liu R G, Koike T (2009). Simultaneous estimation of both soil moisture and model parameters using particle filtering method through the assimilation of microwave signal. J Geophys Res, 114(D15): D15103

Reynolds C, Jackson T, Rawls W (1999). Estimating available water content by linking the FAO soil map of the world with global soil profile database and pedo-transfer functions. American Geophysical Union Fall Meeting, EOS Transactions

Rozelle S, Huang J K, Zhang L X (1997). Poverty, population and environmental degradation in China. Food Policy, 22(3): 229–251

Sridhar V, Elliott R L, Chen F (2003). Scaling effects on modeled surface energy-balance components using the NOAH-OSU land surface model. J Hydrol (Amst), 280(1–4): 105–123

Sridhar V, Elliott R L, Chen F, Brotzge J A (2002). Validation of the NOAH-OSU Land surface model using surface flux measurements in Oklahoma. Journal of Geophysical Research, 107 (D20), 4418

Verburg P H, Overmars K P (2009). Combining top-down and bottom-up dynamics in land use modeling: exploring the future of abandoned farmlands in Europe with the Dyna- CLUE model. Landscape Ecol, 24(9): 1167–1181

Verdin K L, Greenlee S K (1996). Development of continental scale digital elevation models and extraction of hydrographic features. Proceedings of Third International Conference/Workshop on Integrating GIS and Environmental Modeling, National Center for Geographic Information and Analysis, Santa Fe, January, NM, 21–26

Xu T R, Liang S L, Liu S M (2011). Estimating turbulent fluxes through assimilation of geostationary operational environmental satellites data using ensemble Kalman filter. J Geophys Res, 116(D9): D09109

Yang G, Bowling L C, Cherkauer K A, Pijanowski B C, Niyogi D (2010). Hydroclimatic response of watersheds to urban intensity-an observational and modeling based analysis for the White River Basin, Indiana. J Hydrometeorol, 11(1): 122–138

Yang Z L, Niu G Y, Mitchell K E, Chen F, Ek M B, Barlage M, Longuevergne L, Manning K, Niyogi D, Tewari M, Xia Y (2011). The community Noah land surface model with multiparameterization options (Noah-MP): 2. Evaluation over global river basins. Journal of Geophysical Research, 116: D12110

Zhang C L, Chen F, Miao S G, Li Q C, Xia X A, Xuan C Y (2009). Impacts of urban expansion and future green planting on summer precipitation in the Beijing metropolitan area. J Geophys Res, 114 (D2): D02116

Zhang R H, Tian J, Li Z L, Su H B, Chen S H, Tang X Z (2010). Principles and methods for the validation of quantitative remote sensing products. Science China Earth Sciences, 53(5): 741–751

Zhang R H, Tian J, Su H B, Sun X M, Chen S H, Xia J (2008). Two improvements of an operational two-layer model for terrestrial surface heat flux retrieval. Sensors (Basel Switzerland), 8(10): 6165–6187

Zobler L (1986). A world soil file for global climate Modelling. NASA Technical Memorandum #87802